Available online at www.sciencedirect.com
SCIENCE DIRECT®
International Journal of Heat and Mass Transfer 47 (2004) 1037–1052
International Journal of HEAT and MASS TRANSFER
www.elsevier.com/locate/ijhmt

Numerical investigation of a transient free jet resembling a laser-produced vapor jet

G.M. Arshed, S.Z. Shuja, B.S. Yilbas *, M.O. Budair

Department of Mechanical Engineering, King Fahd University of Petroleum and Minerals, P.O. Box 1913, Dhahran 31261, Saudi Arabia

Received 1 April 2003; received in revised form 29 July 2003

Abstract

In the present study, the transiently developing free jet emanating from a laser-impacted surface is considered. The jet velocity profiles are varied with time in connection with the vapor jet velocity profiles emanating from the laser-produced cavity. Consequently, jet expansion from the laser cavity situation is modelled in the simulations. The jet exiting profiles measured previously are employed in the present simulations. Since the thermophysical properties of the laser-produced vapor are unknown, air properties are used for the jet in the simulations. A numerical method employing control volume approach is introduced to discretize governing equations of flow and energy. It is found that in the early period, jet behavior is similar to slowly flowing jets as reported in the literature. The self-similar transient jet behavior occurs as the time progresses; in which case jet exit velocity profiles become similar.

Keywords: Transient; Turbulence; Jet; Laser

1. Introduction

Transient jets and plumes develop in many engineering operations some of which occur in internal combustion engines, spray driers, laser machining of metals, etc. In transient jets, depending upon the magnitude and profile of the jet exiting velocity, a turbulent regime is developed affecting the flow characteristics. Consequently when modeling the jets with high Reynolds number turbulence modeling should be accounted for.

Considerable research studies were carried out to investigate the transient jet [1–3]. Kouros et al. [4] measured the spreading rate of an unsteady turbulent jet. They reported the penetration length and spreading rate of a non-harmonic unsteady jet. The entrainment characteristics of transient gas jets were formulated and presented by Abraham [5]. He indicated that the entrainment rate varied linearly with axial penetration, and the total mass entrainment had a cubic dependence on axial penetration of the gas jet. Experimental investigation of the development of transient jets and evolving jet diffusion flames was carried out by Park and Shin [6] using a high-speed Schlieren photography. They showed that the jet penetration velocity varied with downstream distance and an increase in Reynolds number gave rise to a higher tip penetration velocity. The transient turbulent gaseous fuel jets for diesel engines were examined by Hill and Ouellette [7]. They found that at high nozzle pressure ratios, depending on the jet injection angle, the jet penetration could be consistent with a penetration constant of 3; moreover, at low-pressure ratios, the presence of the wall noticeably retarded the penetration of the jet. The application of a turbulence probability density function to compute an axisymmetric turbulent free jet flow was considered by Chen and Hong [8]. They indicated that the function employed appeared to be more suitable than conventional moment-closure models in terms of revealing turbulence structure.

Laser heating of metals falls into two categories; namely, conduction limited and non-conduction limited heating situations. In non-conduction limited heating process, such as drilling, material undergoes solid

* Corresponding author. Fax: +966-3-860-2949.
E-mail address: factme@saupmoo.bitnet (B.S. Yilbas).

0017-9310/$ - see front matter © 2003 Elsevier Ltd. All rights reserved.
doi:10.1016/j.ijheatmasstransfer.2003.07.026

Nomenclature

A	coefficients of ϕ in Eq. (31)
a	speed of sound (m/s)
c_p, c_v	specific heat at constant pressure and constant volume ($J\,kg^{-1}\,K^{-1}$)
C	various empirical constants in turbulence model
D	jet width (m)
$\tilde{e}$	Favre-averaged specific internal energy ($J\,kg^{-1}$)
E	total specific internal energy including turbulence kinetic energy ($J\,kg^{-1}$)
E_w	wall roughness parameter in Eq. (26)
G	rate of generation of turbulence kinetic energy ($kg\,m^{-1}\,s^{-3}$)
$\tilde{h}$	Favre-averaged specific enthalpy ($J\,kg^{-1}$)
h''	fluctuating component of specific enthalpy ($J\,kg^{-1}$)
H	total specific enthalpy including turbulence kinetic energy ($J\,kg^{-1}$)
k	turbulence kinetic energy ($m^2\,s^{-2}$)
k_{in}	turbulence kinetic energy at the jet inlet ($m^2\,s^{-2}$)
l_m	mixing length (m)
$\dot{m}_{in}$	mass flux at the jet inlet (inlet to control volume) ($kg\,s^{-1}\,m^{-2}$)
M_t	turbulence Mach number
$\dot{M}$	jet momentum flow rate at the jet inlet (inlet to control volume) ($kg\,m\,s^{-2}$)
n	exponent in Eq. (19)
PD	pressure-dilatation ($kg\,m^{-1}\,s^{-3}$)
$\bar{p}$	time-averaged pressure (Pa)
p'	fluctuating component of pressure (Pa)
P	Pee function in Eq. (30)
q_w	wall heat flux ($Watt\,m^{-2}$)
r	distance along the radial direction (m)
r_0	radius of the jet inlet in Eq. (19) (m)
R	gas constant ($J\,kg^{-1}\,K^{-1}$)
$\overline{S}_h$	time-averaged source term in Eq. (4) ($Watt\,m^{-3}$)
S_0	constant in source term in Eq. (31) ($kg\,s^{-1}\,m^{-3}\times[\phi]$)
S_P	coefficient of source term in Eq. (31) ($kg\,s^{-1}\,m^{-3}$)
S_ϕ	arbitrary source term ($kg\,s^{-1}\,m^{-3}\times[\phi]$)
t	time (s)
$\tilde{T}$	Favre-averaged temperature (K)
T''	fluctuating component of temperature (K)
T_{in}	temperature at the jet inlet (K)
T_w	wall temperature (K)
T_p^+	dimensionless temperature at near wall point y_p
T_p	temperature at near wall point y_p (K)
$\tilde{u}$	Favre-averaged axial velocity (m/s)
u''	fluctuating component, of axial velocity (m/s)
u_i, u_j	arbitrary axial/radial velocity (m/s)
$\tilde{u}_i$, $\tilde{u}_j$	arbitrary Favre-averaged axial/radial velocity (m/s)
u_i'', u_j''	arbitrary fluctuating component of axial/radial velocity (m/s)
u_p	resultant tangential velocity (m/s)
u^+	dimensionless resultant tangential velocity
u_0	maximum axial velocity at the jet inlet (m/s)
u_{in}	axial velocity at the jet inlet (inlet to control volume) (m/s)
u_τ	resultant friction velocity (m/s)
$\tilde{v}$	Favre-averaged radial velocity (m/s)
v''	fluctuating component of radial velocity (m/s)
v_{in}	radial velocity at the jet inlet (inlet to control volume) (m/s)
$\widetilde{V}$	Favre-averaged velocity magnitude (m/s)
x	axial distance (m)
x_i, x_j	arbitrary distance (m)
y_p	normal distance from point p to the solid wall (m)
y_p^+	dimensionless normal distance from point p to the solid wall
Z_t	penetration depth/length (m)

Greek symbols

α	closure constants in Eq. (16)
γ	specific heat ratio (c_p/c_v)
δ_{ij}	Kronecker delta
ϵ	dissipation rate of turbulence kinetic energy ($m^2\,s^{-3}$)
ϵ_{in}	dissipation rate of turbulence kinetic energy at the jet inlet ($m^2\,s^{-3}$)
κ	von Karman's constant
μ	laminar dynamic viscosity ($kg\,m^{-1}\,s^{-1}$)
μ_t	eddy viscosity ($kg\,m^{-1}\,s^{-1}$)
$\bar{\rho}$	time-averaged density ($kg\,m^{-3}$)
ρ'	fluctuating component of density ($kg\,m^{-3}$)
σ	Prandtl number
σ_t	turbulent Prandtl number
σ_k, σ_ϵ	turbulence constants in Eqs. (13) and (14)
$\bar{\tau}_{ij}$	time-averaged stress tensor (Pa)
τ_w	wall shear stress (Pa)
ϕ	arbitrary variable
$[\phi]$	unit of arbitrary variable (ϕ)
$\forall$	volume (m^3)

Subscripts

amb	ambient
in	inlet

i, j	arbitrary direction	w	wall
P	a typical node in the computational domain	N, S, E, W	nodes around a control volume
0	maximum	n, s, e, w	interface of a node to its north, south, east, or west
t	turbulent		

heating, melting and evaporation. The evaporating front forms a transient jet emanating outwards from the surface of the substrate material. Consequently, a laser non-conduction limited heating process is involved with melting and cavity formation inside the substrate material and expansion of the evaporated surface. Considerable research studies were carried out to examine the physical processes involved during laser heating process. Laser non-conduction limited heating was considered by Bang and Modest [9]. They investigated the multiple reflection effects on evaporative cutting with a moving continuous wave (CW) laser. They indicated that multi-reflection resulted in increased material removal rates and deeper grooves. The energy transfer rates and penetration depth into the solid during a high energy beam drilling were investigated by Wei and Ho [10]. They showed that non-linear variations in the penetration velocity with energy density occurred and the predictions agreed well with the experimental results.

The transient evaporation model for laser machining was proposed by Modest [11]. He showed that during short-pulsed laser ablation conduction losses were essentially negligible, resulting in substantially larger removal rates than for CW operation. Conduction and advection heat transfer in the solid and liquid metal during laser drilling process was investigated by Ganesh et al. [12]. They formulated the governing equations for conduction and advection and presented a numerical methodology for the solution of governing equations. The scaling laws for thick-section cutting with a chemical oxygen-iodine laser was introduced by Kar et al. [13]. They discussed the influence of cutting speed and cutting gas velocity on the cutting depth and showed the effects of various cutting parameters on the cut feature. A theoretical analysis of the energy balance in the laser-metal interaction zone was carried out by Vladimir and Matsunawa [14]. They indicated that the melt flow in the pool carried away from the interaction zone a significant portion of the absorbed laser power intensity.

However, mainly experimental studies were conducted to explore the above surface phenomenon during laser evaporative heating process, i.e., expansion of the evaporating surface emanating from the free surface of the work piece. This is because of limited information available on the thermophysical properties of the evaporating front. Moreover, the theoretical models developed previously were limited to one-dimensional analysis and did not give insight into the expansion rate of the evaporating front [15]. Consequently, further investigation into a transient jet in relation to laser non-conduction limited heating situation becomes fruitful, since the end product quality (drilled hole or cut shape) is highly dependent upon the above surface phenomenon.

In the present study, high temperature transient jet resembling the laser-produced metal vapor jet is considered. Since the metal vapor ejecting from the surface is at elevated temperature, the air jet temperature is set as 1500 K in the simulations. The velocity profile data obtained from the previous experimental study [16] is employed as jet profile emanating from the surface. Since the thermophysical properties of the metal vapor jet are not known, the air jet is considered as emanating from the surface. Although metal vapor properties differ from the air properties, it is expected that the predictions give qualitative agreement with the actual situation. However, the experimental results for the transient behavior of the jet are not available in the open literature to verify this situation. Moreover, the assumption of air as an ideal gas simplifies the analysis. In order to account for the turbulence, the k–ϵ model is employed. It should be noted that in free shear flows, the flow field can be assumed to be fully turbulent everywhere. Consequently, the k–ϵ model can predict the flow field within a reasonable accuracy [19]. The flow field is simulated numerically.

2. Formulation of the flow and energy equations

2.1. Mean-flow equations

The system in the present study is an air jet emerging into an initially stagnant air surrounding. The flow field is compressible, unsteady, two-dimensional, axisymmetric and turbulent. The governing *Favre-averaged transport equations* [17] can be given in the following form:

Equation of continuity:

$$\frac{\partial \bar{\rho}}{\partial t} + \frac{\partial}{\partial x_i}(\bar{\rho}\tilde{u}_i) = 0 \tag{1}$$

Equation of motion:

$$\frac{\partial}{\partial t}(\bar{\rho}\tilde{u}_i) + \frac{\partial}{\partial x_j}(\bar{\rho}\tilde{u}_j\tilde{u}_i) = \frac{\partial \bar{\rho}}{\partial x_i} + \frac{\partial}{\partial x_j}[(\bar{\tau}_{ij} - \overline{\rho u_j'' u_i''})] \tag{2}$$

where $\bar{\tau}_{ij}$ is a time-averaged stress tensor and is given as follows:

$$\bar{\tau}_{ij} = \overline{\mu\left(\frac{\partial u_i}{\partial x_j}+\frac{\partial u_j}{\partial x_i}\right) - \frac{2}{3}\mu\frac{\partial u_k}{\partial x_k}\delta_{ij}} \tag{3}$$

Energy equation:

$$\frac{\partial}{\partial t}(\bar{\rho}E) + \frac{\partial}{\partial x_j}(\bar{\rho}\tilde{u}_j H) = \frac{\partial}{\partial x_j}\left[\left(\frac{\mu}{\sigma}\right)\left(\frac{\partial \tilde{h}}{\partial x_j}\right) - \overline{\rho u_j'' h''}\right] + \frac{\partial}{\partial x_j}[\tilde{u}_i(\bar{\tau}_{ij} - \overline{\rho u_j'' u_j''})] + \bar{S}_h \tag{4}$$

where the quantities E and H are the total specific internal energy and total specific enthalpy, which include the kinetic energy of the fluctuating turbulent field known as *turbulence kinetic energy* (k), viz.,

$$E = \tilde{e} + \frac{1}{2}\tilde{u}_i\tilde{u}_i + k \tag{5}$$

and

$$H = \tilde{h} + \frac{1}{2}\tilde{u}_i\tilde{u}_i + k \tag{6}$$

where $\tilde{e}$ and $\tilde{h}$ are the Favre-averaged internal energy and Favre-averaged enthalpy, respectively, which are given by;

$$\tilde{e} = c_v\widetilde{T} \tag{7}$$

and

$$\tilde{h} = c_p\widetilde{T} = \tilde{e} + \frac{\bar{p}}{\bar{\rho}} \tag{8}$$

where c_v and c_p are the specific heat at constant volume and constant pressure, respectively. The above Eq. (4) is valid for $k \ll \tilde{h}$.

Equation of state:

$$\bar{p} = \bar{\rho}R\widetilde{T} \tag{9}$$

where R is a gas constant.

2.2. Turbulence equations

2.2.1. Eddy-viscosity and eddy-diffusivity concept

The term $-\overline{\rho u_i'' u_j''}$ in Eqs. (2) and (4) are *Favre-averaged-Reynolds stresses*. It was proposed by Boussinesq that modelling these stresses required the analogy with viscous stresses in laminar flows, i.e., these stresses like viscous stresses can also be put in the following form [17]:

$$-\overline{\rho u_i'' u_j''} = \mu_t\left(\frac{\partial \tilde{u}_i}{\partial x_j}+\frac{\partial \tilde{u}_j}{\partial x_i}\right) - \frac{2}{3}\left(\mu_t\frac{\partial \tilde{u}_k}{\partial x_k} + \bar{\rho}k\right)\delta_{ij} \tag{10}$$

By analogy with Favre-averaged-Reynolds stresses $-\overline{\rho u_j'' u''}$ in Eq. (4) is the turbulent transport of a scalar (enthalpy) and is given by:

$$-\overline{\rho u_j'' h''} = \frac{\mu_t}{\sigma_t}\left(\frac{\partial \tilde{h}}{\partial x_j}\right) \tag{11}$$

where σ_t and μ_t are turbulent Prandtl number and eddy viscosity, respectively. The ratio, μ_t/σ_t by analogy with eddy viscosity, is eddy thermal diffusivity. Experiments in many flows have established that the value of σ_t is often around unity [18]. The turbulent viscosity, μ_t, can be defined by the following relation [19]:

$$\mu_t = C_\mu\bar{\rho}k^2/\epsilon \tag{12}$$

where C_μ is an empirical constant, k is the *turbulence kinetic energy* and ϵ is the *turbulence dissipation rate*. Definitions of these turbulence quantities may be given by the standard *k–ϵ model*.

2.2.2. The standard k–ϵ model

The conservation equations for the turbulence kinetic energy (k) and its dissipation rate (ϵ), in order that the mean-flow equations be closed, can be modelled by the standard k–ϵ model. These conservation equations are:

$$\frac{\partial}{\partial t}(\bar{\rho}k) + \frac{\partial}{\partial x_j}(\bar{\rho}\tilde{u}_j k) = \frac{\partial}{\partial x_j}\left[\left(\frac{\mu_t}{\sigma_k}\right)\frac{\partial k}{\partial x_j}\right] + G - \bar{\rho}\epsilon + \mathrm{PD} \tag{13}$$

similarly ϵ is the *energy dissipation* given by;

$$\frac{\partial}{\partial t}(\bar{\rho}\epsilon) + \frac{\partial}{\partial x_j}(\bar{\rho}\tilde{u}_j\epsilon) = \frac{\partial}{\partial x_j}\left[\left(\frac{\mu_t}{\sigma_\epsilon}\right)\frac{\partial \epsilon}{\partial x_j}\right] + C_1\frac{\epsilon}{k}(G + \mathrm{PD}) - C_2\bar{\rho}\frac{\epsilon^2}{k} \tag{14}$$

where G is the rate of production rate of turbulence kinetic energy, $\rho\epsilon$ is its destruction rate and PD is the pressure-dilatation which is due to the compressibility effect. G and PD are approximated respectively by the following relationships [17]:

$$G = -\overline{\rho u_i'' u_j''}\frac{\partial \tilde{u}_i}{\partial x_j} \tag{15}$$

and

$$\mathrm{PD} = \alpha_1\bar{\rho}(-\overline{\rho u_i'' u_j''})\left(\frac{\partial \tilde{u}_i}{\partial x_j}\right)M_t + \alpha_2\bar{\rho}\epsilon M_t^2 \tag{16}$$

where the values of α_1 and α_2 (closure constants) are 0.15 and 0.2, respectively and M_t is the turbulence Mach number which is defined as:

$$M_t = \left(\frac{2k}{a^2}\right)^{1/2} \tag{17}$$

where a is the speed of sound and is given as:

$$a = (\gamma R\widetilde{T})^{1/2} \tag{18}$$

The standard k–ϵ model contains empirical constants which are assigned the following values:

C_μ	C_1	C_2	σ_k	σ_ϵ	σ_t
0.09	1.44	1.92	1.00	1.30	0.7

In general, the standard k–ϵ model is valid in regions where the flow is entirely turbulent. Close to the solid walls, viscous effects become dominant and such a model does not lead to acceptable predictions. Therefore, wall functions discussed in boundary conditions are used near solid walls.

2.3. Boundary conditions

With reference to Fig. 1(a), five boundary conditions need to be considered, including: *gas inlet*, *unbounded air outlet* (*pressure boundary*), *symmetry axis*, *entrainment boundary*, *and the solid wall*. These are given as follows:

2.3.1. Inlet conditions

The velocity profile at the control volume inlet varies spatially and temporarily due to the resembling of the vapor front velocity generated during the laser heating process. Therefore, the velocity profiles obtained from the previous study [16] are employed for the inlet boundary. Since, the emerging jet is involved with a compressible flow, a mass flux (mass flow rate per unit area) is considered at the inlet, i.e.

$$\dot{m}_{\text{in}} = \bar{\rho} u_{\text{in}} = \bar{\rho} u_0 \left(1 - \frac{r}{r_0}\right)^n, \quad 0 \leqslant r \leqslant r_0 \tag{19}$$

where u_0, r_0 and n are functions of time and are given as follows:

$$u_0 = -3 \times 10^8 \times t^2 - 215718 \times t + 131.25 \text{ (m/s)} \quad 0 \text{ μs} \leqslant t \leqslant 376.92 \text{ μs} \tag{20}$$

$$r_0 = \begin{cases} 4444470 \times t^2 - 0.684 \times t + 10^{-4} \text{ (m)} \\ \quad 0 \text{ μs} \leqslant t \leqslant 23.07 \text{ μs} \\ 0.00052 \text{ (m)} \\ \quad 30.76 \text{ μs} \leqslant t \leqslant 353.84 \text{ μs} \\ 50055 \times t^2 - 29.165 \times t + 0.0035 \text{ (m)} \\ \quad 361.53 \text{ μs} \leqslant t \leqslant 376.92 \text{ μs} \end{cases} \tag{21}$$

$$n = 2 \times 10^7 \times t^2 - 7693.1 \times t + 0.9473 \quad 0 \text{ μs} \leqslant t \leqslant 376.92 \text{ μs} \tag{22}$$

In order to resemble the high temperature of the evaporating surface, the emerging jet temperature is considered as 1500 K and remains constant, i.e.

$$\widetilde{T} = T_{\text{in}} \quad (1500 \text{ K})$$

Values of k and ϵ are not known at the inlet, but some reasonable assumptions can be made. Applying the assumption of local equilibrium (rates of production and dissipation are both in balance) at the inlet gives the following relationships [19,20]:

$$k_{\text{in}} = \frac{1}{C_\mu} l_{\text{m}}^2 \left(\frac{\partial u_{\text{in}}}{\partial r}\right) \tag{23}$$

and

$$\epsilon_{\text{in}} = C_\mu^{1/2} k \left|\frac{\partial u_{\text{in}}}{\partial r}\right| \tag{24}$$

where l_{m} is the mixing length and is given by the following *Nikuradse Formula* [19,20]:

$$\frac{l_{\text{m}}}{r_0} = 0.14 - 0.08\left(\frac{r}{r_0}\right)^2 - 0.06\left(\frac{r}{r_0}\right)^4, \quad 0 \leqslant r \leqslant r_0 \tag{25}$$

The radial velocity component (v_{in}) at this inlet is set to zero.

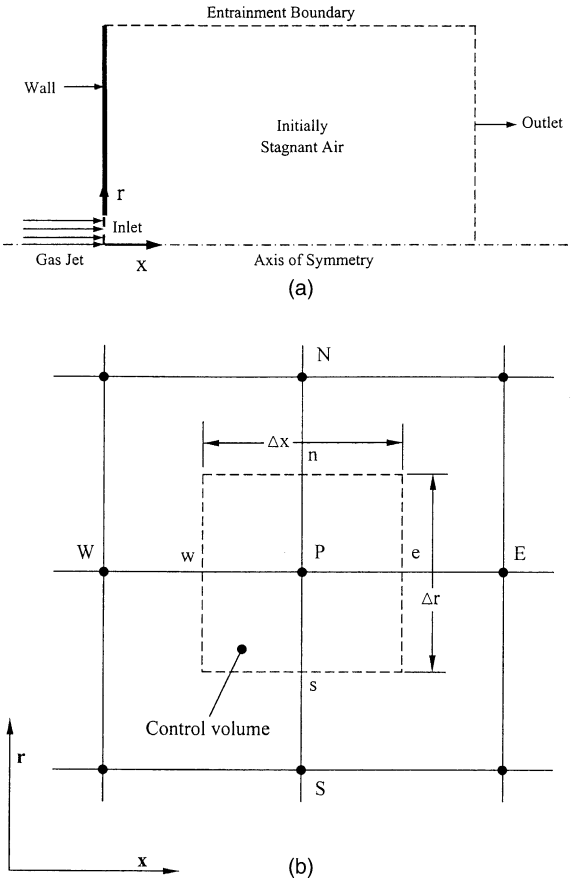

Fig. 1. (a) The solution domain of an axisymmetric transient turbulent air jet emanating from the inlet and emerging into an initially stagnant air surrounding and (b) control volume for the two-dimensional situation.

2.3.2. Outlet

It is considered that the flow extends over a sufficiently long domain so that the pressure boundary is satisfied. Thus;

$$\bar{p} = p_{\text{amb}}$$

The temperature at this boundary is the same as ambient temperature. Moreover, zero values of turbulence properties (k and ϵ) and mean velocities ($\tilde{u}$ and $\tilde{v}$) are used.

2.3.3. Entrainment boundary

The pressure and temperature at this boundary are the same as ambient condition. Zero values of turbulence properties (k and ϵ) and mean–velocity gradients ($\partial\tilde{u}_i/\partial x_j$) are used [18,21].

2.3.4. Symmetry axis

Here the radial derivatives for all mean variables ($\partial\phi/\partial r$) except the radial velocity ($\tilde{v} = 0$) are set to zero. Also $\partial k/\partial r$ and $\partial\epsilon/\partial r$ and are set to zero at the symmetry axis [18,21].

2.3.5. Solid wall

At a solid boundary the no-slip condition applies so that both mean and fluctuating velocities (u, v, u'', v'') are zero but the dissipation rate (ϵ) is finite. The equations need to be integrated through the viscous sublayer when the boundary conditions are specified at the wall. But this process requires many grid points in the viscous sublayer because the velocity gradients are very sharp here and this means additional computational load. Furthermore, since the Eqs. (13) and (14) assume high Reynolds number (because the laminar viscosity (μ) is neglected from these equations), they are not applicable in the viscous sublayer where μ is not insignificant. Therefore, the *Universal Law of the Wall* is introduced to avoid integration in the viscous sublayer. This law connects the wall conditions such as wall shear stress and heat flux, and temperature to the dependent variables just outside the viscous sublayer. This law gives the following logarithmic relationship between the resultant tangential velocity (u_p) and the dimensionless normal distance (y_p^+) from point p to the solid wall:

$$u_p = \frac{u_\tau}{\kappa} Ln(E_w y_p^+), \quad 30 < y_p^+ < 500 \tag{26}$$

where κ ($=0.41$) is von Karman's constant, E_w ($=$ 9.8 for smooth wall) is the wall roughness parameter and u_τ are the resultant friction velocity. u_τ and y_p^+ are given in their respective order by the following relations:

$$u_\tau = \left(\frac{\tau_w}{\bar{\rho}}\right)^{1/2} \tag{27}$$

$$y_p^+ = \frac{\bar{\rho}\tau_w y_p}{\mu} \tag{28}$$

where y_p is the normal distance from point p to the solid wall and τ_w is the wall shear stress.

In addition, measurements of turbulence kinetic energy budgets indicate that the production of turbulence kinetic energy is equal to the dissipation in the log-law region (local equilibrium). Using this assumption and eddy-viscosity equation, Eq. (12), one can develop the following wall functions:

$$k = \frac{u_\tau^2}{\sqrt{C_\mu}}, \qquad \epsilon = \frac{u_\tau^3}{\kappa y_p} \tag{29}$$

For heat transfer the universal near wall temperature distribution at high Reynolds number is used [18]:

$$T_p^+ = -\frac{(T_p - T_w)c_p\bar{\rho}u_\tau}{q_w} = \sigma_t\left[u^+ + P\left(\frac{\sigma}{\sigma_t}\right)\right] \tag{30}$$

where T_p^+ is the dimensionless temperature at near wall point y_p, T_p is the temperature at near wall point y_p, T_w is the wall temperature, q_w is the wall heat flux, u^+ ($=u_p/u_\tau$) is dimensionless resultant tangential velocity and P is the *Pee-function*, a correction function dependent on the ratio of laminar to turbulent Prandtl numbers [18].

The solid wall is assumed to remain at constant temperature ($T_w = 400$ K) with no radiation losses taken into account in the simulation.

2.4. Initial conditions

The initial conditions are imposed before the jet emerges into the control volume. Therefore, initially stagnant air at ambient temperature (300 K) and pressure (atmospheric pressure) is considered in the control volume.

2.5. Properties

The thermal properties of air were considered to vary with pressure and temperature and the ideal gas law was applied. The compressibility effect is accommodated during the simulations.

3. Numerical procedure

3.1. Control volume approach

From the differential equations governing the relevant variables, such as velocity, pressure, temperature, etc. algebraic equations are derived for the grid-point values of the variables. The calculation domain is divided into sub-domains or control volumes such that there is one control volume around a grid point. The differential equation is integrated over the control volume to yield the corresponding discretization equation.

The discretization procedure is given in [18]. The first order upwind scheme is introduced in the discretization process. The details of the analysis is given in [18,22]. The finite difference equation expressing ϕ_P, the value of ϕ at location P, in terms of the values at the nearest neighboring nodes in space and time is given below:

$$(A_P - S_P)\phi_P = A_N\phi_N + A_S\phi_S + A_E\phi_E + A_W\phi_W + A_P^0\phi_P^0 + S_0 \quad (31)$$

where $A_P = \sum_n A_n$, $A_P^0 = \rho_P^0 \Delta\forall/\Delta t$ and S_0, S_P are deduced from the source term (S_ϕ). Equations of this kind are written for each of the variables $\bar{p}$, $\tilde{u}$, $\tilde{v}$, k, ϵ, and $\widetilde{T}$ at every computational cell.

The nodes of a typical grid for two dimensions are labeled as P, N, S, E, and W. This is shown in Fig. 1(b).

3.2. Calculation procedure

If the pressure field which appears as a major part of the source term for the momentum equations is assumed, then Eq. (31), written for velocities at each grid node, yields a closed set of algebraic equations, but the resulting velocity field may not satisfy the continuity relation. This problem of determining the pressure and satisfying continuity may be overcome by adjusting the pressure field so as to satisfy continuity. A staggered grid arrangement is used in which the velocities are stored at a location midway between the grid points, i.e., on the control volume faces. All other variables including pressure are calculated at the grid points. This arrangement gives a convenient way of handling the pressure-velocity linkage through the continuity equation and is known as the SIMPLE (semi-implicit method for pressure-linked equations) algorithm. The details of this algorithm are given in [18,22].

3.3. Computation

The computer program used for the present simulation can handle a non-uniform grid spacing. Along the radial direction fine uniform grid spacing is allocated at the inlet (inlet to control volume) while gradually increased spacing is considered away from it. Along the axial direction grid spacing is fine near the inlet and the wall but it is gradually increasing. The grid generated in the present study is shown in Fig. 2. The number of grid planes used in the radial direction is 40 while 50 grid planes are used in the axial direction, thus making a total of 2000 grid points. The grid independence test results for pressure and velocity are shown in Figs. 4 and 5, respectively. It may be observed that for 55×45 grid points the results are almost in agreement with the results of 50×40 grid points, i.e., the maximum pressure and velocity magnitude differences are less than 0.1% (two curves are overlapping in the figures). It should be noted that the grid independent test results are not shown for all time steps due to large number of curves in the figure. Moreover, the jet exit velocity at this time ($t = 192.30$ μs) is almost developed (does not change much with progressing time).

Six variables are computed at all grid points; these are: the two velocity components, the local pressure, the two turbulence quantities and the temperature.

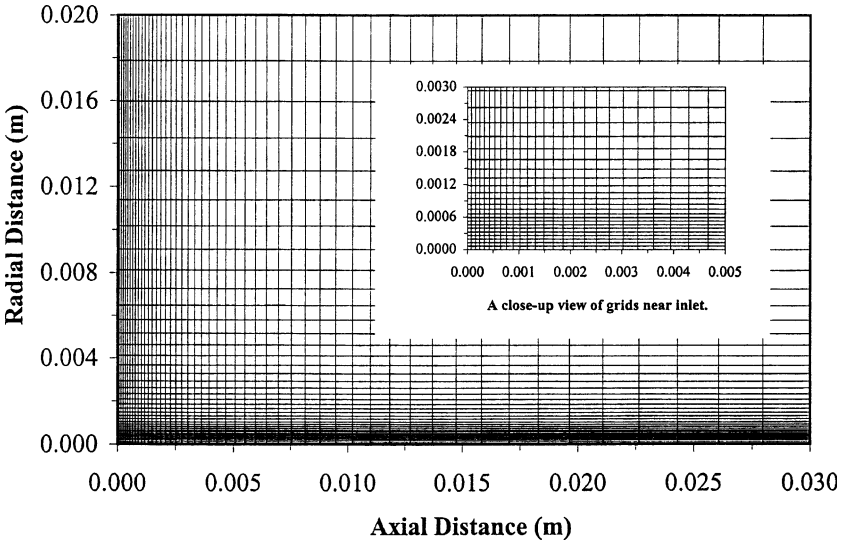

Fig. 2. Computational domain for grid independent solution of an axisymmetric transient turbulent air jet exiting into an initially stagnant air surrounding (grid size 50×40).

4. Results and discussions

A transient jet emanating from the solid surface is simulated to resemble the laser induced evaporation process. Since the actual vapor properties are not known, air at 1500 K is considered as an ejecting gas. The vapor jet profile emanating from the cavity was measured experimentally [16]; consequently, jet velocity profiles obtained from measurements are employed as jet exit conditions in the simulations. Moreover, jet profile varied with time, this situation is also accommodated in the simulations. Fig. 3 shows the jet exit (inlet to the control volume) profiles.

Since the flow field presented in the present study resembles laser induced vapor expansion from the cavity, there are no experimental and theoretical studies to validate the present predictions. Consequently, the simulation conditions are changed to validate present predictions with the experimental results obtained previously for the transient flow situation [4]. In order to secure the validity of the predictions, the boundary and initial conditions are set in accordance with the experimental conditions, which are given in [4]. Fig. 6 shows jet penetration length with time predicted and obtained from the experiment [4]. The penetration length was measured from the pipe exit to the tip of the jet, and the tip was inspected visually from photographs. It can be observed that both results are in agreement and the difference is within ~14%. The error bars are associated with the experimental error, which was reported as 3.5%.

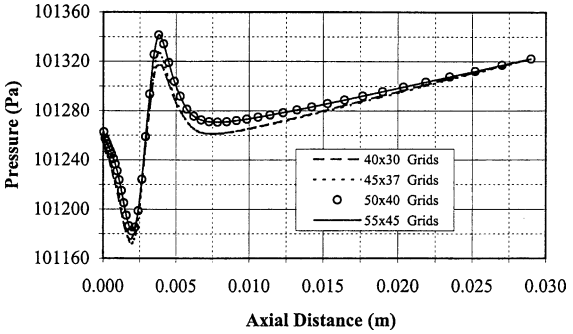

Fig. 4. Grid independent test for pressure along the symmetry axis at $r = 0$ m and $t = 192.30$ μs.

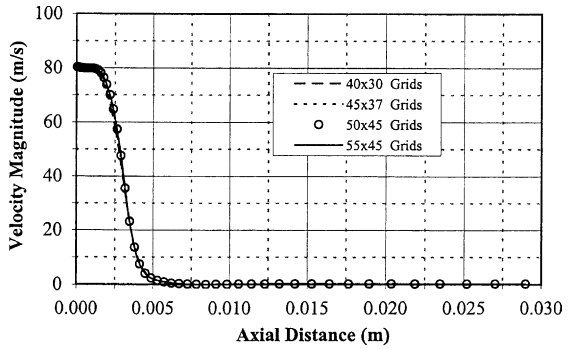

Fig. 5. Grid independent test for velocity magnitude along the symmetry axis at $r = 0$ m and $t = 192.30$ μs.

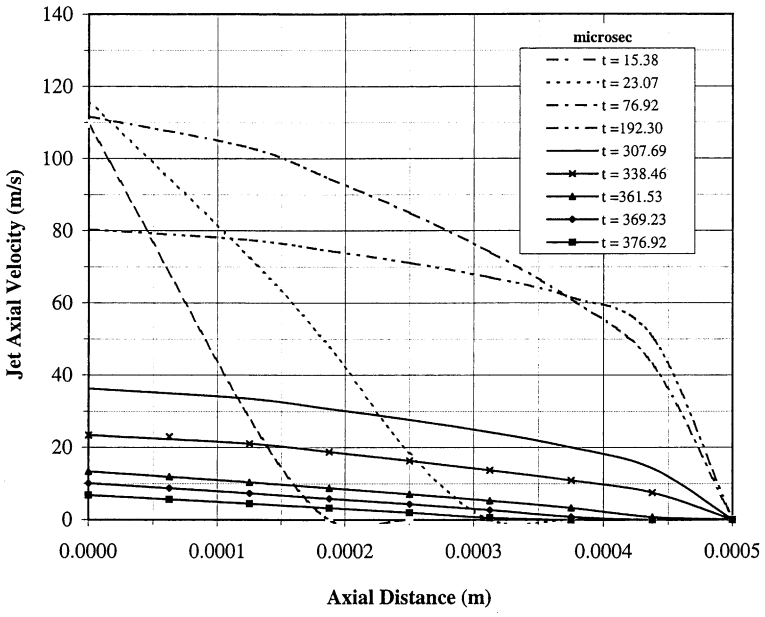

Fig. 3. Profiles of jet axial velocity at the gas jet inlet for various times [16].

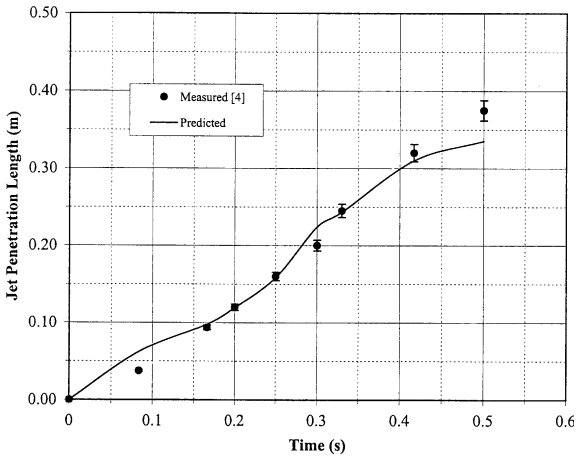

Fig. 6. Comparison of numerical predictions with the experimental data for the case of unsteady turbulent jet entering the water tank [4]. The error bars are associated with the experimental error (3.5%) as indicated in the previous study [4].

Fig. 7(a) and (b) show velocity vectors in the region close to the jet inlet-expansion region as well as in the radially extended and axially contracted region. The jet expansion results in the development of the circulation cell in the region next to the jet outer surface. This is because of the flow entrainment in this region. The orientation of the circulation cell changes as jet expansion progresses. This is mainly because of the jet inlet velocity profile, which changes spatially with time (Fig. 3). Therefore, the fluid entrainment varies with time. In the early period ($t \leqslant 76.92$ μs), jet expands axially as well as radially; however, as the time progresses axial expansion dominates over the radial expansion. This is due to: (i) the pressure builds up at the jet front during the initial expansion period and (ii) the jet inlet velocity profile develops radially with time (Fig. 3). In this case, as the jet velocity profiles become similar, the axial expansion of the jet is considerable.

Fig. 8 shows the velocity magnitude contours while Fig. 9 shows its variation along the symmetry axis as time variable. In the early period, jet expansion is not considerable and as the time progresses jet expands radially first then expands further along the axial direction. This is because of the jet exit velocity profile, which develops radially with time as well as still air resistance opposing the jet expansion in the axial direction. Flow entrainment is evident after $t = 307.69$ μs, in this case, the outer velocity contours differ than those corresponding to earlier time period. Although the jet penetration extends in the axial direction, velocity magnitude reduces considerably with progressing time (Fig. 9). This occurs because of the jet exit velocity profile, where the mean velocity reduces significantly (Fig. 3).

The turbulence kinetic energy is high at the jet exit in the early period. This can be observed from Fig. 10, in which turbulence kinetic energy along the symmetry axis is shown. This is because of the jet exit velocity profile. It should be noted that the turbulence kinetic energy is associated with the jet exit velocity profile (Eq. (23)). The turbulence kinetic energy reduces at jet exit; however, it attains relatively high values along the symmetry axis during $76.92 \leqslant t \leqslant 192.30$ μs. As the time progresses, its magnitude reduces and does not alter much along the symmetry axis. Moreover, changes in jet exit velocity profile results in changes in velocity magnitude along the symmetry axis. This, in turn, causes large variation in turbulence kinetic energy, which was also observed in the previous study [23].

Fig. 11 shows pressure variation along the symmetry axis as time variable. The sharp change is observed in the early period of jet penetration, which is due to the initial ambient resistance to the jet expansion. As the time progresses, jet expands into its surrounding first resulting in low pressure in the region next to the jet exit and then due to retarding action of the jet front the pressure rises in the region close to the jet front. As the time progresses further, pressure in the jet settles as if it decays from jet exit to jet front.

Fig. 12 shows temperature profiles along the symmetry axis as time variable while Fig. 13 shows temperature contours at different times. Temperature profiles follow almost the profiles of velocity magnitude. This is more pronounced in the early periods. In this case, convective heat transfer from the jet surface to its ambient is small due to short period of time. As the time progresses, temperature profiles extend into the jet ambient as follows the jet expansion. When the jet exit profiles become similar in magnitude and shape, the extension of the temperature profiles into the ambient becomes similar to the case observed for the unsteady jets [7].

Fig. 14 shows the dimensionless ratio (ratio of the jet width to penetration depth) while the logo in the figure shows temporal behavior of penetration depth. The penetration depth in the early period is low as compared to jet width in the radial direction. Moreover, as the time progresses, penetration depth becomes larger and the radial expansion of the jet becomes less than the penetration along the jet symmetry axis. However, as the time progresses further, jet expansion results in almost self-similar region as noted in the previous study [7]. In this case D/Z_t attains almost steady decay, which is more pronounced after 150 μs. Moreover, it was shown that for a fixed jet exit velocity profile a self-similar transient jet could be resulted [7]. Since the gas inlet velocity profiles are varied in the present simulations (in order to resemble vapor ejection from the laser-produced cavity), a self-similar

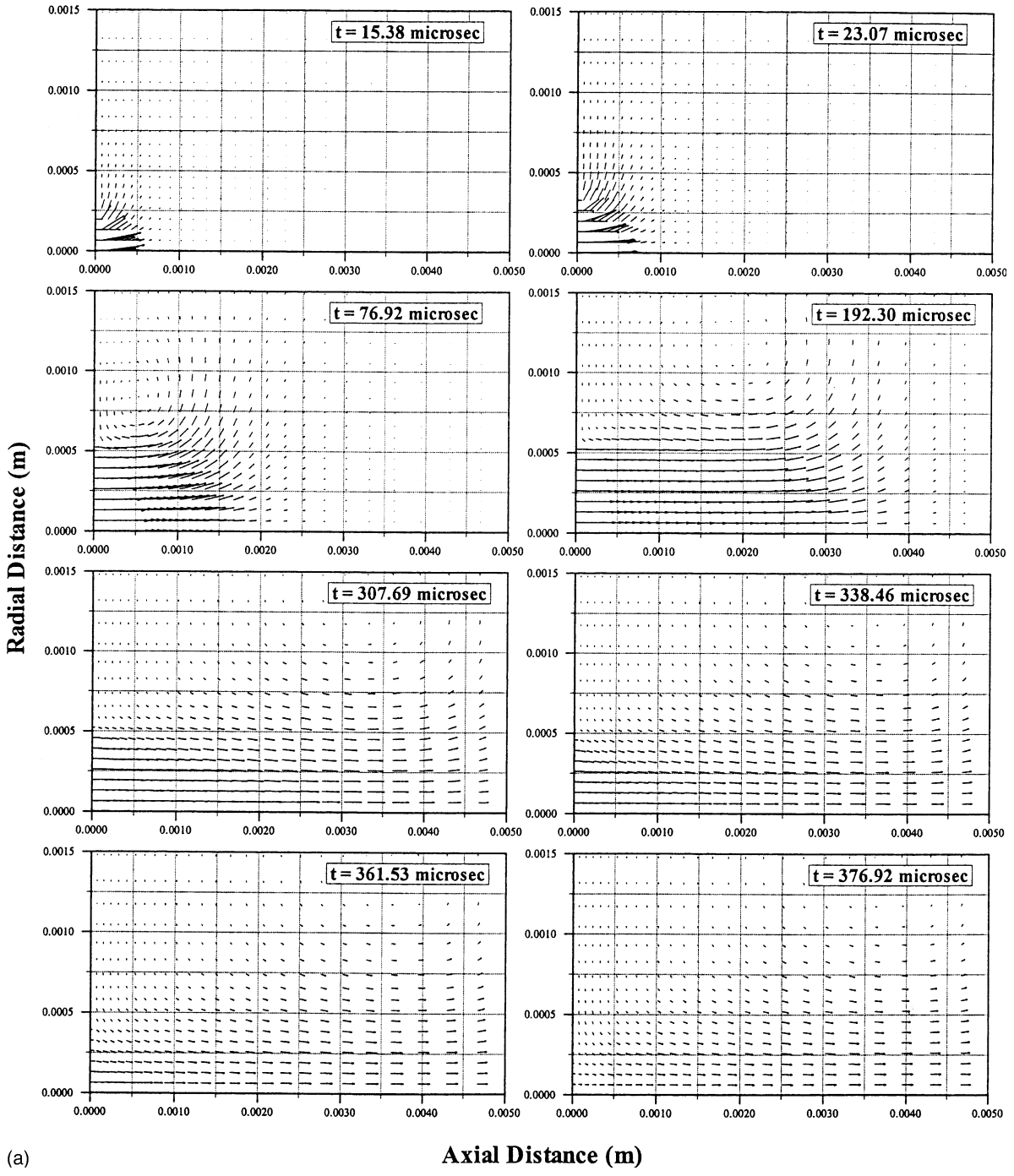

(a)

Fig. 7. (a) Time development of velocity vector plots for an axisymmetric transient turbulent air jet close to the jet inlet-expansion region. (b) Time development of velocity vector plots for an axisymmetric transient turbulent air jet in the radially extended and axially contracted region.

region is not observed clearly in the initial period, except when the jet exit profiles become similar. This corresponds to time period of 150 μs.

Fig. 15 shows the ratio of penetration depth (Z_t) to 1/4 power of specific momentum $\left(\dot{M}/\bar{\rho}\right)$. It should be noted that the penetration number is given as [7]:

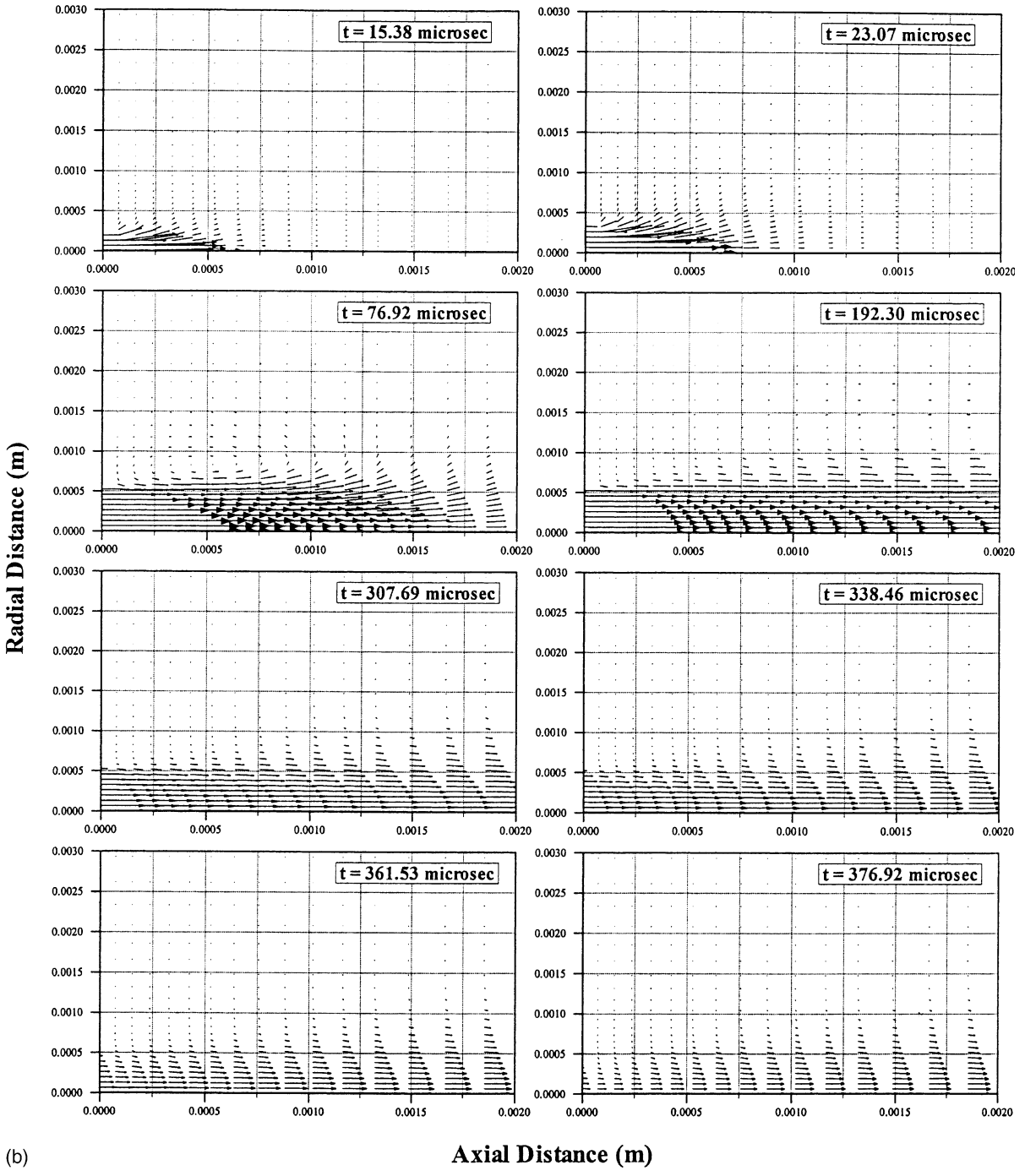

(b)

Fig. 7. (*continued*)

$$\frac{Z_t}{\left(\dot{M}/\bar{\rho}\right)^{1/4} \times t^{1/2}} = f(D/Z_t) \tag{32}$$

It was reported that for slow flow transient jets, the penetration number remains constant [7]. It can be observed from the figure that the penetration number increases linearly with $\sqrt{t}$ for $\sqrt{t} \leqslant 12$ and beyond this time it changes vastly, i.e. constant slope of the curve indicates the constant rate of increase in penetration number. Consequently, in the early period jet behavior is

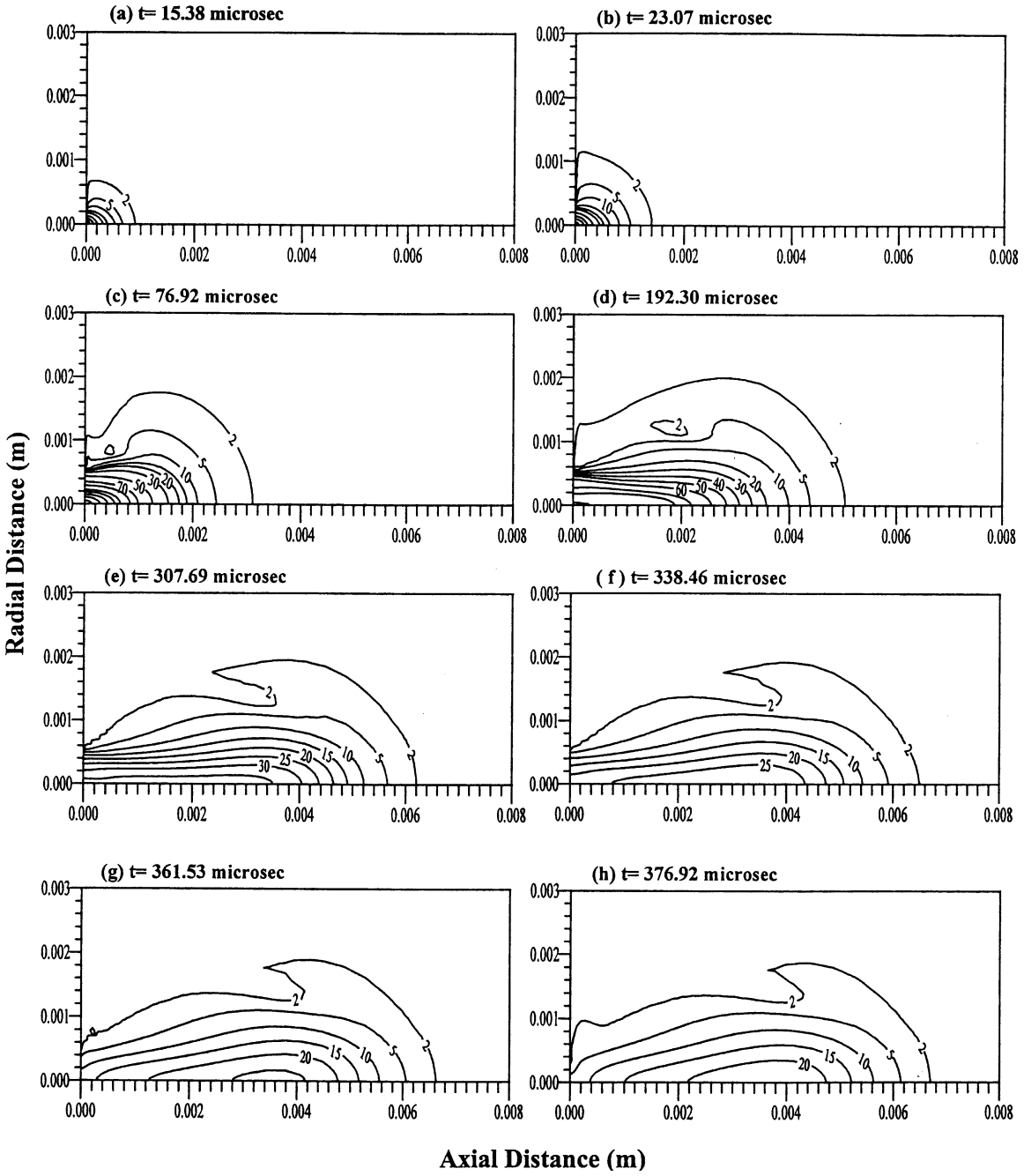

Fig. 8. Time development of velocity magnitude contours for an axisymmetric transient turbulent air jet exiting into initially stagnant air.

similar to that corresponding to slow flow jet expansion. In this case, the penetration depth is low and the momentum of the jet is high. As the time progresses, some portion of the jet momentum is lost due to viscous effect. This in turn reduces the specific momentum of the jet. Moreover, as the time progresses, the jet penetration rate reduces due to the retarding pressure force build up in the region next to the jet front. Although the jet penetration rate reduces with progressing time, the jet momentum reduces more swiftly because of the viscous dissipation. Therefore, the rate of momentum loss is considerably higher than the reduction in penetration

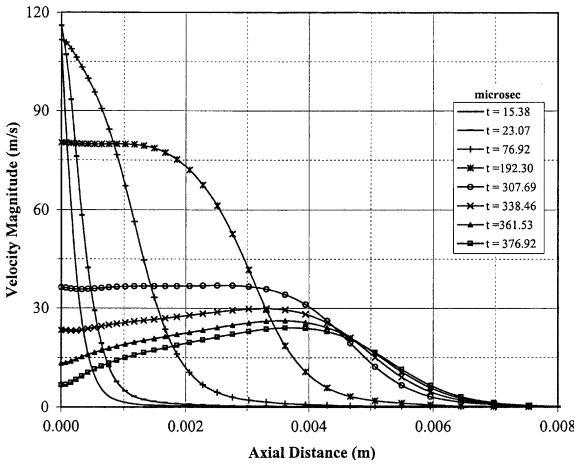

Fig. 9. Temporal variation of velocity magnitude along the jet symmetry axis at $r = 0$ m for an axisymmetric transient turbulent air jet exiting into initially stagnant air.

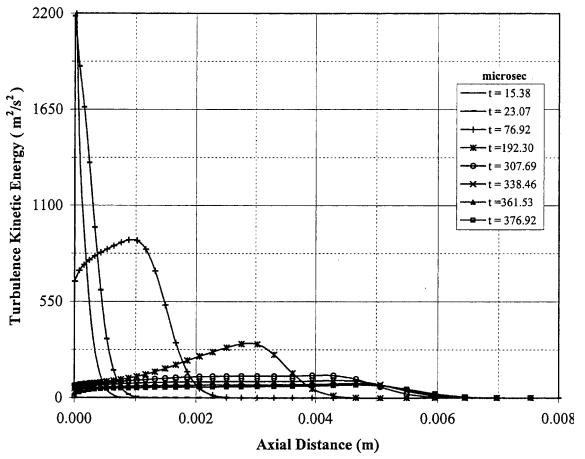

Fig. 10. Temporal variation of turbulence kinetic energy along the jet symmetry axis at $r = 0$ m for an axisymmetric transient turbulent air jet exiting into initially stagnant air.

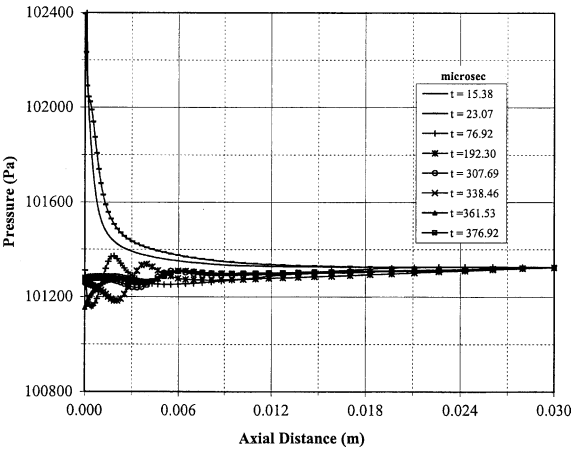

Fig. 11. Temporal variation of pressure along the jet symmetry axis at $r = 0$ m for an axisymmetric transient turbulent air jet exiting into initially stagnant air.

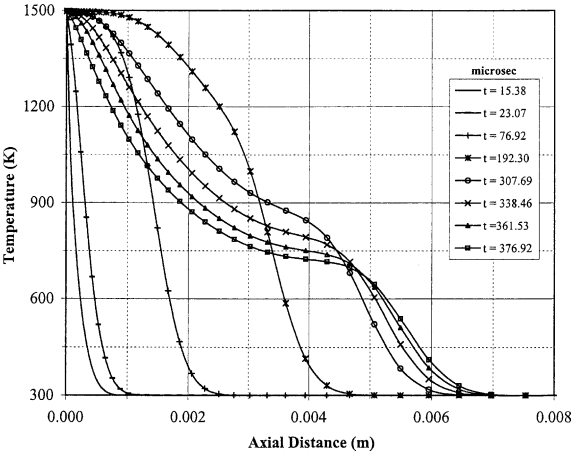

Fig. 12. Temporal variation of temperature along the jet symmetry axis at $r = 0$ m for an axisymmetric transient turbulent air jet exiting into initially stagnant air.

rate. This, in turn, results in rapid rise of slope of the curve in the figure for $\sqrt{t} \geqslant 12$.

5. Conclusions

Transiently developing jet emanating from a free surface is considered to resemble the vapor jet behavior ejected from the laser-produced cavity. Since the thermophysical properties of laser-produced vapor is not known, air is considered as fluid in the simulations. The jet exiting velocity profiles (jet velocity profiles onset of exiting the cavity) employed are obtained from the previous experimental study. This enables us to simulate the actual laser-produced cavity exiting conditions. A numerical scheme employing control volume approach is employed when simulating the flow situations. It is found that in the early period temperature profiles follow the velocity profiles and the convective heat transfer from the jet surface to its ambient is small. During this period jet expands more radially than it does axially. As the time progresses, the jet width to jet penetration depth ratio reduces. Once the jet exit velocity profiles become almost similar, self-similar transient jet behavior is resulted. The specific conclusions derived from the present study can be listed as follows:

(1) Changes in jet exit velocity profiles alter the turbulence kinetic energy generation along the symmetry

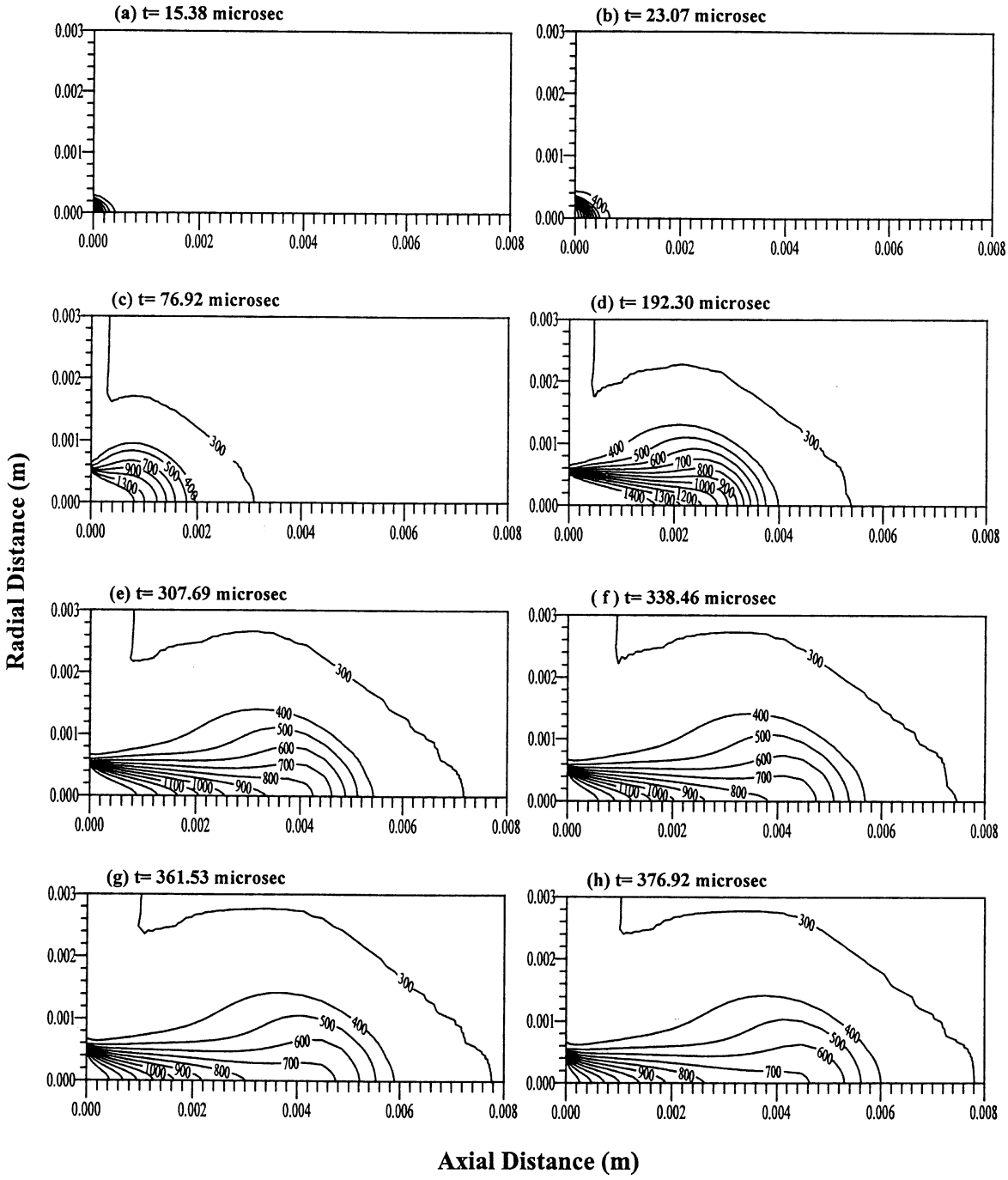

Fig. 13. Time development of temperature contours for an axisymmetric transient turbulent air jet exiting into initially stagnant air.

axis. Moreover, very small change in velocity magnitude results in large change in turbulence kinetic energy.

(2) In the early period the ratio of jet expansion in the axial direction to the one-fourth power of jet specific momentum increases linearly with the square root of time, i.e., penetration number increases steadily. In this case, jet behaves similar to those observed for slow flow jets. As time progresses, the rate of momentum dissipation due to viscous dissipation becomes

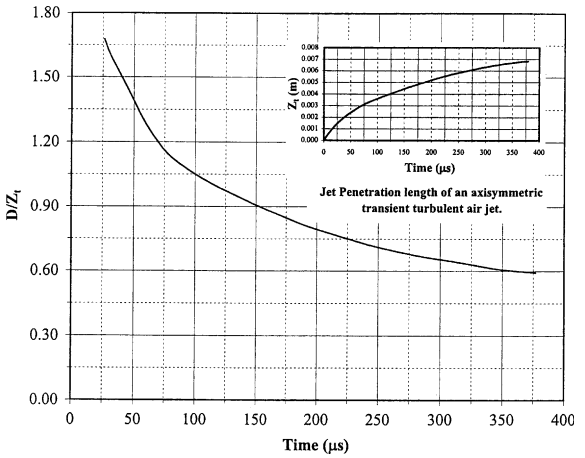

Fig. 14. Ratio of jet width to penetration length with time for an axisymmetric transient turbulent air jet exiting into initially stagnant air.

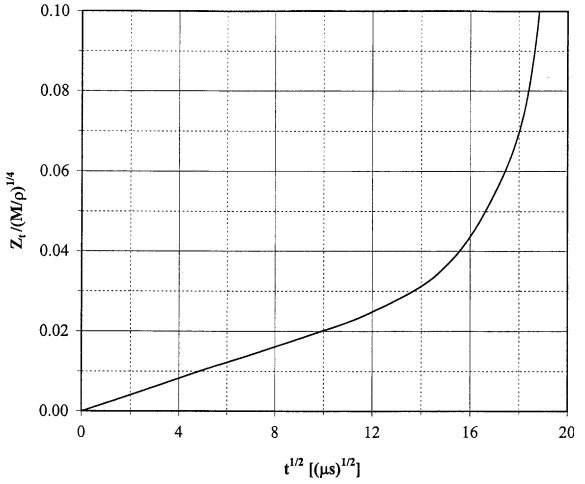

Fig. 15. Penetration rate of an axisymmetric transient turbulent air jet exiting into initially stagnant air.

high and the penetration number increases rapidly. This is observed for $\sqrt{t} \geqslant 12$ in the present case.

Acknowledgements

The authors acknowledge the support of King Fahd University of Petroleum and Minerals. Dhahran, Saudi Arabia for this work.

References

[1] K. Bremhorst, P.G. Hollis, Velocity field of an axisymmetric pulsed, subsonic air jet, AIAA J. 28 (12) (1990) 2043–2049.

[2] R.E. Breidenthal, The turbulent exponential jet, Phys. Fluid 29 (8) (1986) 2346–2347.

[3] F. Fang, B.L. Sill, Experimental investigation of unsteady submerged axisymmetric jets, J. Hydraul. Eng. 113 (5) (1987) 663–669.

[4] H. Kouros, R. Medina, H. Johari, Spreading rate of an unsteady turbulent jet, AIAA J. 31 (8) (1993) 1524–1526.

[5] J. Abraham, Entrainment characteristics of transient gas jets, Numer. Heat Transfer, Part A 30 (1996) 347–364.

[6] J. Park, H.D. Shin, Experimental investigation of the developing process of an unsteady diffusion flame, Combust. Flame 110 (42) (1997) 67–77.

[7] P.G. Hill, P. Ouellette, Transient turbulent gaseous fuel jets for diesel engines, ASME J. Fluid Eng. 121 (1999) 93–101.

[8] M.-H. Chen, Z.-C. Hong, A pdf description of turbulent axisymmetric free jet flow, ASME J. Fluid Eng. 121 (1999) 73–79.

[9] S.Y. Bang, M.F. Modest, Multiple reflection effects on evaporative cutting with a moving CW laser, J. Heat Transfer 113 (1991) 663–669.

[10] P.S. Wei, J.Y. Ho, Energy considerations in high-energy beam drilling, Int. J. Heat Mass Transfer 33 (10) (1990) 2207–2217.

[11] M.F. Modest, Three-dimensional, transient model for laser machining of ablating/decomposing materials, Int. J. Heat Mass Transfer 39 (2) (1996) 221–234.

[12] R.K. Ganesh, A. Faghri, Y. Hahn, A generalized thermal modelling for laser drilling process—I. Mathematical modeling and numerical methodology, Int. J. Heat Mass Transfer 40 (14) (1997) 3351–3360.

[13] A. Kar, J.A. Rothenflue, W.P. Latham, Scaling laws for thick-section cutting with a chemical oxygen-iodine laser, J. Laser Appl. 9 (1997) 279–286.

[14] V. Semak, A. Matsunawa, The role of recoil pressure in energy balance during laser materials processing, J. Phys. D: Appl. Phys. 30 (1997) 2541–2552.

[15] B.S. Yilbas, A.Z. Sahin, R. Davies, Laser heating mechanism including evaporation process initiating laser drilling, Int. J. Mach. Tools Manufact. 35 (7) (1995) 1047–1062.

[16] B.S. Yilbas, G.M. Arshed, H.I. Acar, Investigation into laser produced evaporating front characteristics in relation to laser drilling, Lasers in Engineering 13 (1) (2003) 65–74.

[17] D.C. Wilcox, Turbulence Modeling for CFD, DCW Industries Inc., 2000, pp. 223–252 (Chapter 5).

[18] H.K. Versteeg, W. Malalasekera, An Introduction to Computational Fluid Dynamics, The Finite Volume Method, Longman Scientific and Technical, 1995 (Chapter 5).

[19] W. Rodi, Turbulence Models and Their Application in Hydraulics—A State of the Art Review, Presented by the IAHR-Section on Fundamentals of Division II: Experimental and Mathematical Fluid Dynamics, February 1984.

[20] R.S. Amano, H. Brandt, Numerical study of turbulent axisymmetric jets impinging on a flat plate and flowing into an axisymmetric cavity, ASME J. Fluid Eng. 106 (1984) 410–417.

[21] S.Z. Shuja, B.S. Yilbas, M.O. Budair, Gas jet impingement on a surface having a limited constant heat flux area: Various turbulence models, Numer. Heat Transfer, Part A 36 (1999) 171–200.

[22] S.V. Patankar, Numerical Heat Transfer and Fluid Flow, Series in Computational Methods in Mechanics and Thermal Sciences, McGraw-Hill Book Company, 1980.

[23] B.S. Yilbas, S.Z. Shuja, M.O. Budair, Stagnation point flow over a heated plate: consideration of gas jet velocity profiles, AJSE 27 (2002) 91–116.